SAND2021-5956R

# LIDAR For Heliostat Optical Assessment Final Report

Charles Q. Little[1, a)], Daniel E. Small[3, b)], Julius Yellowhair[3, c)]

[1, 2]*Sandia National Laboratories, P.O. Box 5800, Albuquerque, NM 87185 USA.*
[3]*Gryphon Technologies, 2309 Renard Pl SE #120, Albuquerque, NM 87131 USA.*

[a)] cqlittl@sandia.gov
[b)] desmall@sandia.gov
[c)] jey422@gmail.com

## GOALS AND OBJECTIVES

This project has sought to develop new uses for surveying-quality Light Detecting and Ranging (LiDAR) 3D scanning sensors in the automatic/autonomous assessment of optical errors in largescale concentrating solar power heliostat fields. Past experiments have demonstrated the ability of a 3D-LiDAR to acquire highly accurate point cloud measurements across several Sandia NSTTF heliostats. The goal of this project is to expand upon this work to see if and how it can be used in large commercial heliostat fields.

The project task list included the following:

- Procure LiDAR & evaluate accuracy and software API
- Write software for autonomous segmentation and error analysis
- Deploy the system at suitable sites testing and evaluation.
- Compare and contrast the accuracy of the scan to other methods.
- Assess LiDAR method for repeatability and accuracy.
- Produce a written report with appropriate peer-review of progress and results

This paper will be the final report, covering the whole of the project. After the **Introduction**, the report will be organized corresponding to the task list.

## INTRODUCTION

Sandia Labs has had a long-standing role in research and development of solar energy systems; in particular, concentrated solar power technology, with heliostats outfitted with multiple facets targeting sunlight at a target on a central tower. Figure 1 shows the Sandia National Laboratories National Solar Thermal Test Facility (NSTTF) solar tower and heliostat field located in Albuquerque, New Mexico, USA. Figure 2 shows a single heliostat in that field. Clearly, the performance of the heliostat field can be impacted by mirror canting errors, tracking errors, and soiling. Each of these issues will reduce the sunlight hitting the target and therefore the performance of the field.

**Figure 1. Sandia NSTTF solar tower and heliostat field**

**Figure 2. Sandia NSTTF heliostat**

Sandia has in the past and continues to develop tools for heliostat focusing and canting enhancement (HFACET) [1 - 2]. In regard to a current project (UFACET) [3], we were asked to see if LiDAR scanning could be used to locate the position of a facet in 3D, primarily as a test to acquire truth data. The conventional wisdom says LiDAR scanning does not work on shiny surfaces. So, we proposed putting checkerboard targets on the corners of the facets. We have software that can automatically find checkerboard targets, and this would give us a simple way to capture four points on the facet and use those to calculate the plane of the facet. The normal to the plane would give us the pointing angle. The position and normal of multiple facets on a heliostat would provide the data to calculate the canting angles. We tested the targets at 10 meters, and then went to the field and placed them on the heliostat facet corners. Our experiment worked better than expected. Figure 3 shows the checkboard target (a), the resulting LiDAR scan data in the lab at 10 meters (b), and the resulting LiDAR scan data of the targets placed on the facet corners of a heliostat (c).

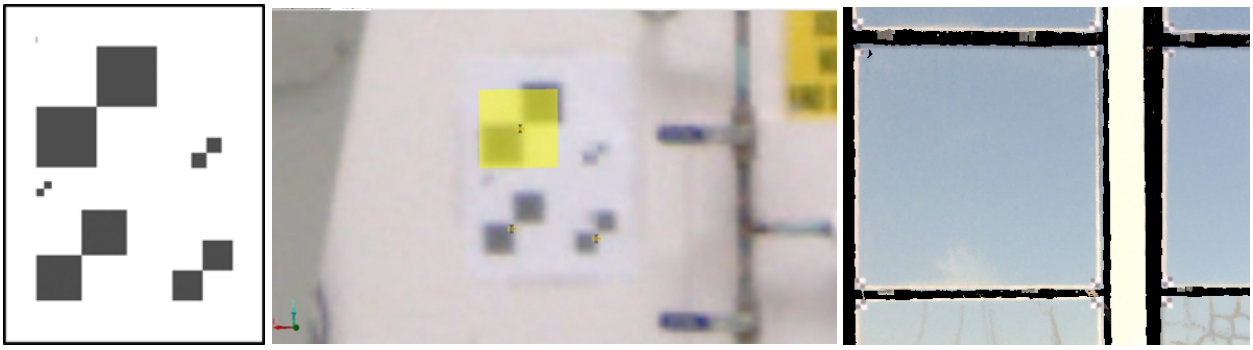

**Figure 3. a) checkerboard target, b) scan results on wall at 10 meters, c) scan result on heliostat facet in field**

As seen in the figure, the mirror surface is manifestly visible in the scan data. This was a ‘eureka’ moment. It meant we did not need the checkerboard target at all. We could use the entire surface of the facet to know its location relative to its neighbors as well as fit a plane to find its pointing angle.

## PROCURE LIDAR & EVALUATE ACCURACY AND SOFTWARE API

### FARO S70 LiDAR sensor

For our project, we used a FARO Focus S70 laser scanner [4], as shown in figure 4. This is a scanning LiDAR which spins a ranging laser about the horizontal and vertical axes to create 3D point clouds and weighs 10 pounds. For a typical 45-million-point scan, the corresponding 3D point spacing is 6 mm at 10 meters. This corresponds to 40,000 points on a square 1.2-meter facet. The 70 refers to the range limit of 70 meters.


**Figure 4. FARO Focus S70 3D scanner**

### LiDAR Scanning of heliostats

A LiDAR scanner uses a laser to detect the distance from the scanner to objects in its surroundings. The technology used is time-of-flight (or phase shift). These scanners typically are mounted on a stationary platform, like a tripod, to maintain a fixed position while scanning. (They can be mounted on moving platforms, but that requires additional localization hardware to combine the data to a single coordinate frame). While the base of the scanner is fixed, the unit itself uses a rotating mirror to scan vertically and turns the unit to scan horizontally. In this way, data can be captured of an entire area; 360 degrees horizontally and near that (minus the mounting for ~300 degrees) vertically. Resolutions are around ± 2 mm. Practical range measurements can be read from ½ to 50 meters or more. The output is a series of locations or points in space. These points come from the reflection of the laser on the surfaces seen by the sensor. Location here refers to the x-y-z coordinate position of the point relative to the scanner. Most surfaces will adequately reflect laser light, but not all; very shiny and non-reflective surfaces (coating, black matte) and no surface (open sky and out of range) will have false returns or no return at all. Data consists of values per point: x-y-z position and usually a laser return intensity. In addition, many 3D scanners are co-equipped with visual cameras, and can acquire color (RGB) values for each point. It is not unusual for the output to contain tens to hundreds of million points per scan. Scan times vary with point density, but a typical 50-million-point scan can take < 5 minutes.

## Mirror Surface Results

As mentioned in the **Introduction,** we were very surprised to discover that in addition to the checkerboard targets, the mirror surface was also detected by the LiDAR scanner. Figure 5 is a full image of the scan data. Figure 6 is a photo image from the same heliostat. We found that mirrors with near reflections of background did not return the surface. Note in particular the area where the heliostat in front of this one is reflected in the lower center facets. Note also the upper mirror surfaces are present; these have sky reflected in them. For further detail, figure 7 shows a closeup of the scan data (this is from the lower left corner of the center facet. Note the density of the data.

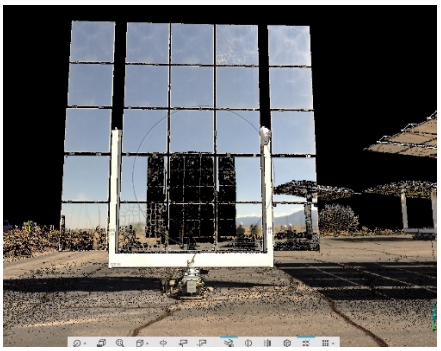

**Figure 5. Full LiDAR scan of heliostat**

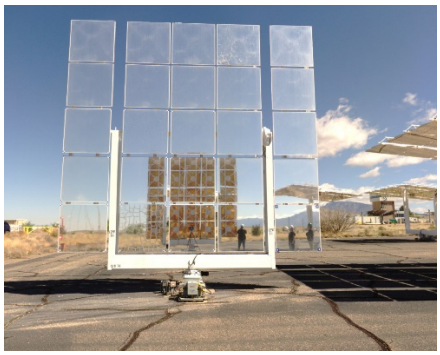

**Figure 6. Photo of heliostat**

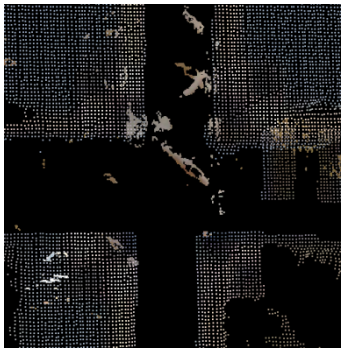

**Figure 7. Closeup of scan data**

## Soiled versus Clean Surfaces

The assumption that was made is the scanner is actually picking up data from the dust or soiling on the mirror surface. The test this theory, we cleaned a half of one of the facets of a heliostat and scanned it. Figure 8 is the result. It is even obvious we did not clean it very well. Close visual inspection also showed most of the mirrors had a dust layer.

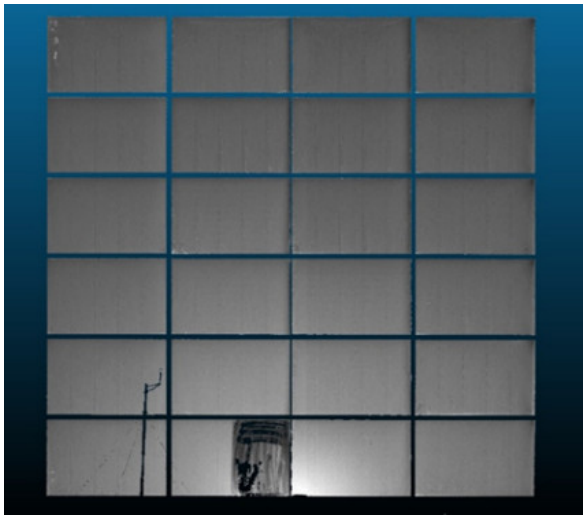

**Figure 8. Heliostat scan with partially clean facet on bottom row**

When we first made this proposal, it was based on taking data of a few heliostats at the NSTTF at Sandia, and at the Crescent Dunes Solar Energy Project in Nevada, all of which returned dense point clouds off the mirror surfaces remarkably well. At the time, we believed that the normal accumulation of dust on the mirror surface was enough to generate good returns. We did not realize how this might be a problem until the mid-fall of 2019 when the NSTTF test engineer used a common technique to clean all the mirrors simultaneously. This involves waiting for the right kind of weather; a dense wet snowstorm of 4 to 6 inches was forecast. As the storm began, the mirrors were oriented to face the sky. After the thick coat of snow accumulated on the horizontal facets, the heliostats were tilted in elevation to allow the snow to rapidly slide off the mirrors, taking months of accumulated soiling and dust with it. This resulted in mirrors that were very clean across the entire field. Figure 9 shows the results of scanning these clean mirrors. As you seen from the lower images, clean mirrors (seen on the left) do not scan anywhere near as well as soiled ones (seen on the right). The NSTTF heliostat design stows the mirrors upside down, which we believe is unique in large solar fields. This means that dust will take longer to adhere to the mirror surface.

Since clean mirrors could pose a major limitation to our system, we successfully experimented with artificially soiling the mirrors by spraying a cornstarch and water mixture on the heliostat. This artificial soil can be easily washed off. The mirrors on the right in figure 9 were sprayed with this mixture.

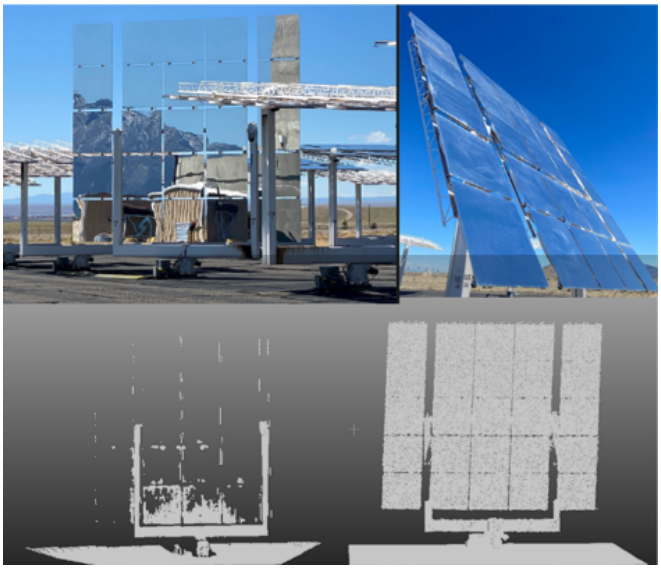

**Figure 9. Clean and soiled heliostat scans**

**Scanner Evaluation for Accuracy**

The advertised accuracy of the FARO S70 includes a range resolution of ± 2 mm, with a range limit of ½ to 70 meters. To evaluate this, we use the RMS value calculated in a plane fit. Planes were used because the method used throughout this project was to use planar fits of the heliostat mirror facets to get numerical values to measure the mirror angles, also called canting angles. Figure 10 shows a segmented point cloud of a facet. Figure 11 shows this data with a plane fit to

it, using a point-cloud evaluation software called CloudCompare [5]. Figure 12 shows the point cloud from a side view. The RMS error of the plane fit, from the software, is around 1.2 mm, indicating the range resolution is what is advertised.

**Figure 10. Segmented points**

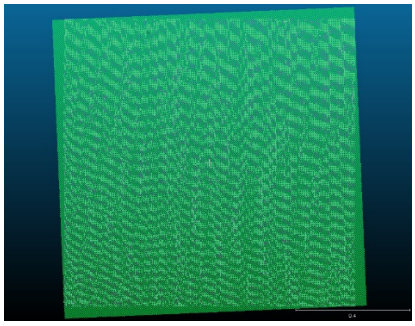

**Figure 11. Plane fit to points**

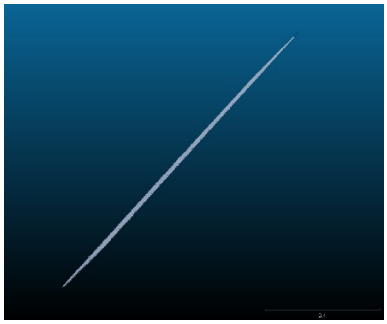

**Figure 12. Segmented points from side**

## Scanner Software API Analysis to Meet Requirements of Project

Automation of the data acquisition and processing of the LiDAR data is an intrinsic goal of this project. Before making the final purchase of the scanning system, we requested that the company (FARO) provide us with their software Application Programmer's interface (API) so that it could be evaluated for its ability to provide the automation capabilities required. In figure 13 we excerpt the parts of the API that support our conclusion that the software API they provide had enough flexibility to accomplish the required task.

```
ScanCtrlSDK
{
// this variable reports the progress as a percentage of the total from 0 to 100
int ScanProgress;
// this variable reports whether the scanner can be remotely configured and triggered
enum RemoteScanAccessStatus RemoteScanAccess;
// these next four variables determine the angles that the scanner will acquire data within
double VerticalAngleMin;
double VerticalAngleMax;
double HorizontalAngleMin;
double HorizontalAngleMax;
// this variable allows fine-grained control of the resolution of the point cloud produced
int Resolution;
//This variable allow you to set the specific base file name of the data being produced
string_t ScanBaseName;
// this variable tells you the current number of the file being written. This combined with the
scan
based above is enough to reconstruct the current file name being written.
int ScanFileNumber;
// this variable returns the current horizontal angle
double HorizontalAngle;
// These functions give a remote client the capability of starting, stopping, and pausing the
current
scan
int startScan ( );
int stopScan ( );
int shutDown ( );
int pauseScan ( );
};
```

**Figure 13. FARO API support for autonomous operation**

Software was written that takes advantage of the capabilities of the FARO Scanner API to remotely trigger a scan via Wi-Fi. In November 2019 we conducted 10 remote scans over the course of one morning. The scanner was moved around to multiple locations within 100 feet of a laptop running the API client. As soon the scanner was stable on its tripod (immediately after

setting it down on a flat surface), the scan was remotely triggered via software and the wireless connection.

We were also able to query the scanner's built-in GPS unit, reading it multiple times while the system was scanning. This allows for GPS averaging, which can increase the accuracy of the position estimate of the sensor head.

Lastly, we were able to use a remote file transfer protocol (FTP) to transfer the sensor data files wirelessly off the sensor head.

Given this level of automation in the API and other wireless services provided by the Faro S70 LiDAR Scanner, we are confident that this system supports the deliverables and milestones of this project.

## SOFTWARE FOR AUTONOMOUS SEGMENTATION AND ERROR ANALYSIS

### Canting Angle Estimation Processing Steps

Given that we can scan the facet mirror surface, we set out to find the canting angles of individual facets. We begin with a full scan of the heliostat, which usually includes the ground around it and other objects in the scan area (see figure 14). Each point has an xyz value, and we can order the z values to estimate and remove the ground (see figure 15). We then isolate the desired heliostat from its neighbors or other objects by using connected component analysis (also called blob detection) as shown in figure 16. We assume we will know the geometry of the heliostat and use it as a template to separate the individual facets. The heliostats we have examined are laid out in a square grid with ample facet separations, so we are using only the 2D separation distances. We accomplish this by using the major axis of the isolated heliostat, using a bounding box algorithm [6] to then translate the data to the X-Y axis. This allows us to use the distance between facet layout of the heliostat to separate each facet. The facet scan data may contain extraneous data. This can be from the support structure that is sometimes scanned through the gaps between facets. An example is shown in figure 17. It is also common for scanning edge effects to give false data. This occurs because the laser beam hitting the edge of objects has a finite dot size, and sometimes partially illuminates more than one surface as it spills over, causing a skirting effect. These bad points can be filtered out. We use two methods. The first uses the same z ordered filter used for the ground finder; the facet is translated to lie in the x-y plane, and the z ordered, with outliers above and below removed. Figure 18 shows an example. Another method to filter the facet is to fit a plane and toss points further away from the plane. Both of these methods suppose outliers are in fact relatively far from the vast majority of the points, which are on the plane.

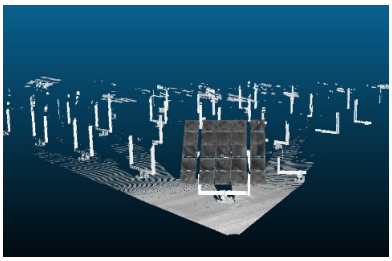

**Figure 14. Full heliostat scan**

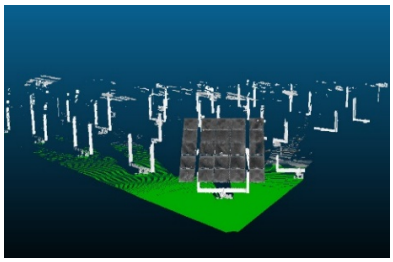

**Figure 15. Estimating ground**

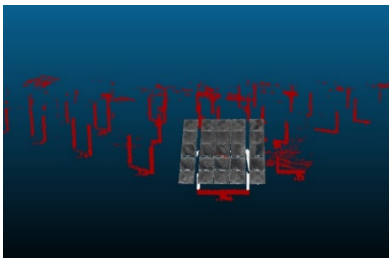

**Figure 16. Isolate neighboring objects**

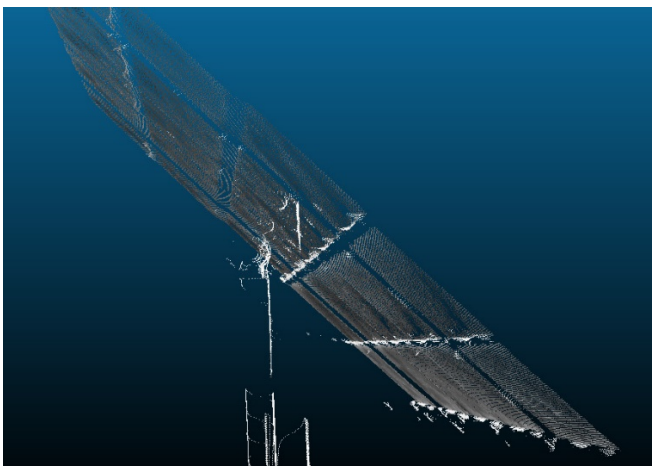

**Figure 17. Extraneous scan data on facets**

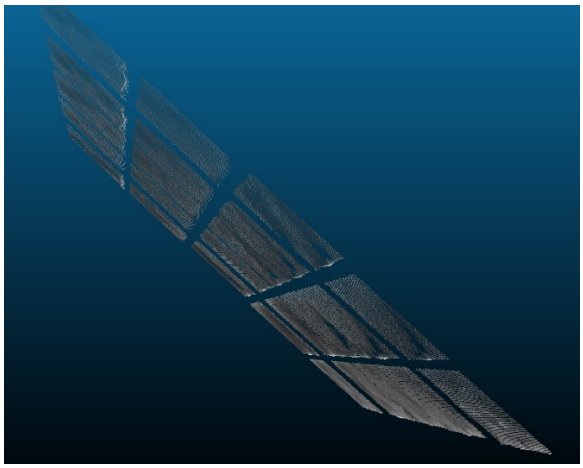

**Figure 18. Filtered facet data**

## Canting Angle Calculation

Finally, with clean facet information, the data is fit to a plane. This is where the LiDAR scan brings a significant advantage. While our LiDAR unit has a range resolution of 2 mm, the planar estimate error is reduced by 1 over the square root of the number of points. In our case, this can be upwards of 100,000 points per facet. The process subtracts the centroid of data (i.e. translating the facet points to the origin) and uses the Singular Value Decomposition method to find the planar normal, which is used as the facet direction vector. This method is described in [7]. The canting angle must be relative to something, and we pick the center facet as the control vector and compare each facet normal to the center facet normal. Figure 19 shows the facets as color coded to show they are indeed separate objects. Figure 20 shows these vectors displayed from the heliostat scan, with the vector originating at the centroid of the facets. Canting angles are reported as azimuth and elevation. A sample of the canting angle difference is shown in Table 1. Figure 21 shows this process in a flowchart.

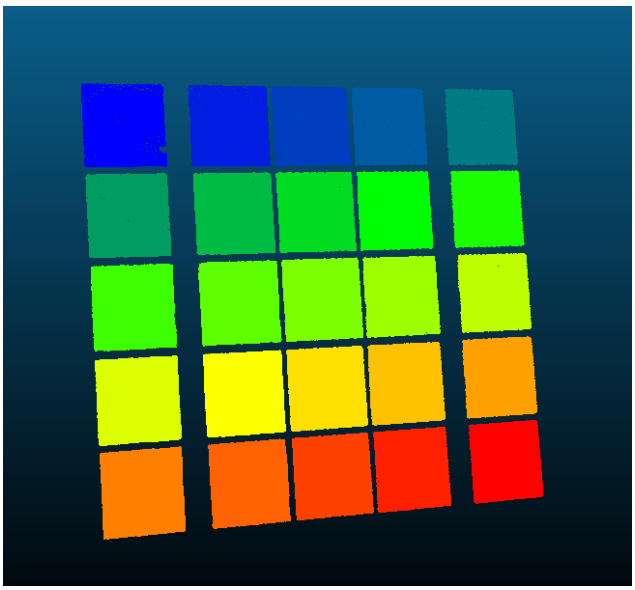

**Figure 19. Separated facets**

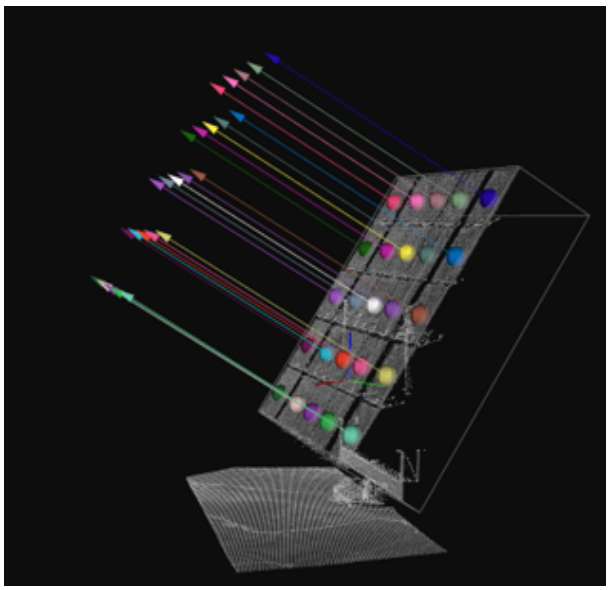

**Figure 20. Canting angles shown with heliostat scan data**

**Table 1. Canting Angle in Azimuth and Elevation**

| facet | facet-base | azimuth deg | elevation deg |
|---|---|---|---|
| 0 | 12 | -0.85459 | -0.53853 |
| 1 | 12 | -0.36427 | -0.52065 |
| 2 | 12 | 0.010802 | -0.63388 |
| 3 | 12 | 0.43217 | -0.53439 |
| 4 | 12 | 0.830944 | -0.55784 |
| 5 | 12 | -0.81569 | -0.25099 |
| 6 | 12 | -0.3692 | -0.29616 |
| 7 | 12 | -0.02272 | -0.26412 |
| 8 | 12 | 0.379161 | -0.25115 |
| 9 | 12 | 0.865491 | -0.26393 |
| 10 | 12 | -0.80935 | -0.07156 |
| 11 | 12 | -0.32628 | -0.02171 |
| 12 | 12 | 0 | 0 |
| 13 | 12 | 0.438819 | -0.00707 |
| 14 | 12 | 0.920358 | 0.008213 |
| 15 | 12 | -0.81405 | 0.378211 |
| 16 | 12 | -0.35875 | 0.386876 |
| 17 | 12 | -0.01381 | 0.343378 |
| 18 | 12 | 0.467871 | 0.353971 |
| 19 | 12 | 0.857984 | 0.357246 |
| 20 | 12 | -0.83984 | 0.709131 |
| 21 | 12 | -0.344 | 0.688654 |
| 22 | 12 | 0.046421 | 0.641184 |
| 23 | 12 | 0.42366 | 0.661934 |
| 24 | 12 | 0.791243 | 0.670158 |

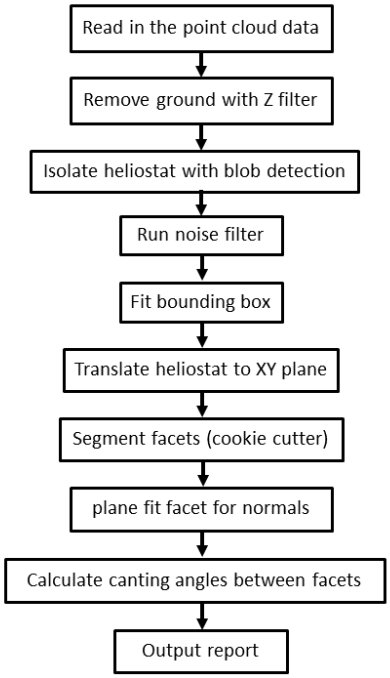


**Figure 21. Flowchart of scan to facet processing**

## Output report

The output report currently contains identification information, followed by the processed facet data. This includes the point count per facet, the planar normal vector, the centroid, and then the azimuth and elevation values in absolute degrees. This is followed by a similar assessment of the heliostat as a whole, by averaging all the facet data for the calculations. Finally, a list of facet azimuth and elevation angle comparisons is added to represent the canting angle difference. This again compares each facet to a facet base, usually the center facet, which is considered the boresight mirror. Table 2 shows a sample report.

**Table 2. Sample heliostat optical error report**

```
# input data file: nstrf0416-9W1-145.pcd
# parameter file: con

. Sample heliostat optical error report
figNSTTF_front.txt
# date-time: Thu Apr 30 14:44:07 2020
# input point cloud size: 3207607
# heliostat point cloud size: 486383
# minimum facet cloud size: 500
# plane fit with SVD
# facet_num, point_count, points_in_fit, normal_x, normal_y, normal_z, center_x, center_y, center_z, aximuth(deg), elevation(deg)
0, 12259, 12259, 0.740231, -0.460442, 0.489951, -11.067164, 6.798945, 50.782494, 31.882674, 29.337329
1, 12268, 12268, 0.736134, -0.466678, 0.490223, -10.240294, 8.078716, 50.778030, 32.372996, 29.355214
2, 11895, 11895, 0.733877, -0.472010, 0.488499, -9.572914, 9.111989, 50.776669, 32.748069, 29.241986
3, 11100, 11100, 0.729674, -0.476930, 0.490014, -8.904441, 10.153380, 50.771839, 33.169437, 29.341475
4, 10084, 10084, 0.726504, -0.482108, 0.489657, -8.090216, 11.433681, 50.763039, 33.568211, 29.318027
5, 14871, 14871, 0.737821, -0.459639, 0.494319, -10.539797, 6.456377, 49.676197, 31.921582, 29.624870
6, 14751, 14751, 0.734546, -0.465583, 0.493634, -9.715022, 7.734216, 49.673553, 32.368072, 29.579702
7, 14261, 14261, 0.731485, -0.469867, 0.494120, -9.046503, 8.769232, 49.672726, 32.714550, 29.611746
8, 13254, 13254, 0.728077, -0.474925, 0.494317, -8.377692, 9.807187, 49.669907, 33.116428, 29.624716
9, 11830, 11830, 0.724112, -0.481149, 0.494123, -7.557472, 11.087881, 49.667633, 33.602758, 29.611930
10, 18256, 18256, 0.736453, -0.458900, 0.497039, -9.977321, 6.086709, 48.575085, 31.927914, 29.804306
11, 18134, 18134, 0.732193, -0.464860, 0.497794, -9.156831, 7.363856, 48.576107, 32.410989, 29.854156
12, 17646, 17646, 0.729375, -0.468920, 0.498122, -8.482693, 8.404494, 48.576000, 32.737267, 29.875862
13, 16002, 16002, 0.725814, -0.474526, 0.498015, -7.815036, 9.442798, 48.570168, 33.176087, 29.868789
14, 14135, 14135, 0.721689, -0.480536, 0.498247, -6.990407, 10.719379, 48.570866, 33.657625, 29.884075
15, 22159, 22159, 0.733156, -0.456762, 0.503835, -9.464880, 5.755703, 47.440823, 31.923222, 30.254074
16, 21803, 21803, 0.729439, -0.462533, 0.503966, -8.644181, 7.029284, 47.438366, 32.378519, 30.262738
17, 21015, 21015, 0.726963, -0.467122, 0.503310, -7.971779, 8.069524, 47.436749, 32.723457, 30.219240
18, 19107, 19107, 0.722933, -0.473166, 0.503470, -7.302105, 9.106152, 47.435181, 33.205139, 30.229833
19, 16793, 16793, 0.719670, -0.478062, 0.503519, -6.473185, 10.383201, 47.440239, 33.595252, 30.233108
20, 26512, 26512, 0.730879, -0.454887, 0.508816, -8.936647, 5.405741, 46.341507, 31.897427, 30.584993
21, 25956, 25956, 0.727069, -0.461292, 0.508508, -8.113950, 6.679357, 46.340523, 32.393265, 30.564516
22, 25095, 25095, 0.724263, -0.466464, 0.507795, -7.441372, 7.724310, 46.339348, 32.783689, 30.517046
23, 22549, 22549, 0.721022, -0.471121, 0.508107, -6.769758, 8.763090, 46.335815, 33.160927, 30.537796
24, 19276, 19276, 0.717924, -0.475697, 0.508230, -5.935774, 10.033005, 46.343063, 33.528511, 30.546020
# heliostat 431011, 431011, 0.728953, -0.469937, 0.497781, -0.000012, -10.000047, 0.059659, 32.808790, 29.853323
# (facet normal angle comparison) facet, facet-base, x_angle_deg, y_angle_deg
0, 12, -0.854593, -0.538533
1, 12, -0.364271, -0.520648
2, 12, 0.0108019, -0.633876
3, 12, 0.43217, -0.534387
4, 12, 0.830944, -0.557835
5, 12, -0.815685, -0.250992
6, 12, -0.369196, -0.29616
7, 12, -0.0227172, -0.264117
8, 12, 0.379161, -0.251146
9, 12, 0.865491, -0.263932
10, 12, -0.809354, -0.0715565
11, 12, -0.326278, -0.0217063
12, 12, 0, 0
13, 12, 0.438819, -0.00707266
14, 12, 0.920358, 0.0082133
15, 12, -0.814046, 0.378211
16, 12, -0.358749, 0.386876
17, 12, -0.0138106, 0.343378
18, 12, 0.467871, 0.353971
19, 12, 0.857984, 0.357246
20, 12, -0.83984, 0.709131
21, 12, -0.344002, 0.688654
22, 12, 0.0464214, 0.641184
23, 12, 0.42366, 0.661934
24, 12, 0.791243, 0.670158
```

## DEPLOY THE SYSTEM AT SUITABLE SITES TESTING AND EVALUATION.

### Repeatability Study -- From Multiple Angles

One way to test the reliability of our proposed system is to take multiple data sets of the same stationary heliostat from several sensor positions. Since the facets will not have moved, their relative positions to each other should be the same. A heliostat at the NSTTF (9W1) was scanned from three different locations. The point clouds are shown in figure set 22.

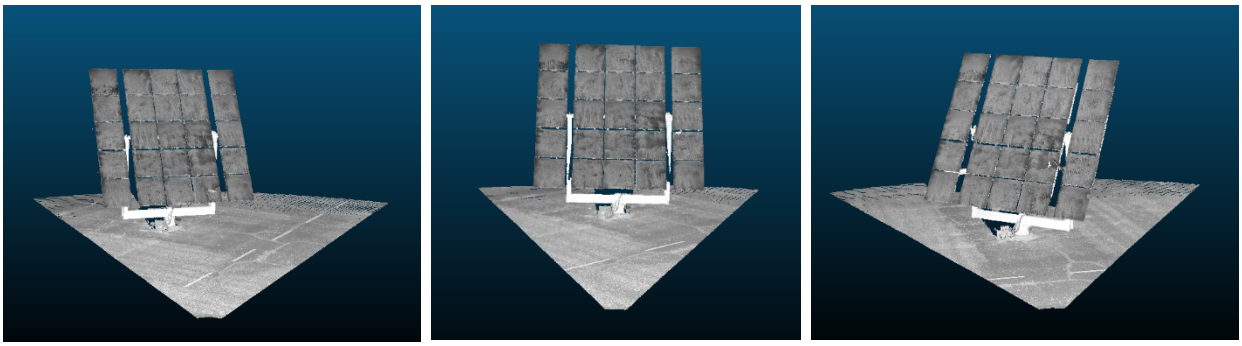

**Figure 22. Point cloud scans of heliostat 9W1, from three scanner positions; left, center, right**

Table 3 shows the azimuth-elevation comparisons for the three data collections. While not exact, the data shows good close matches. There were some extenuating circumstances of the data collection; the scans were taken on a windy day (10-12mph, gusting to 20mph). It is known that wind does affect the positioning of the heliostat. The primary errors are only seen on the outer facets in the azimuth, which are more prone to movement due to the support structure of the heliostat. This could also be a function of the relative azimuth angle to the scanner. A repetition of this experiment on a day without wind should clear up the issue. If it is the wind, then we would need to establish a good wind speed threshold to warn against data collection. We believe that the wind is a much more likely suspect due to the lack of significant error in the elevation angle, which falls just within the repeatability target of 0.25 mrad, at 0.2452 mrad.

**Table 3. Contrast of Azimuth Elevation comparisons (in degrees) for repeated data collections**

| | 9W1-145 | | 9W1-146 | | 9W1-147 | | Std Dev | Std Dev |
|---|---|---|---|---|---|---|---|---|
| facet | Azimuth | Elevation | Azimuth | Elevation | Azimuth | Elevation | Azimuth | Elevation |
| 0 | 0.8572 | -0.5410 | 0.6920 | -0.6440 | -0.7947 | -0.5080 | 0.909793 | 0.070939 |
| 1 | 0.3707 | -0.5219 | 0.4331 | -0.5208 | -0.2059 | -0.5187 | 0.352298 | 0.001626 |
| 2 | -0.0133 | -0.6372 | -0.1433 | -0.6931 | -0.0100 | -0.6101 | 0.076026 | 0.042325 |
| 3 | -0.4322 | -0.5394 | -0.3074 | -0.5118 | 0.4383 | -0.4842 | 0.470711 | 0.0276 |
| 4 | -0.8328 | -0.5606 | -0.8031 | -0.5840 | 0.8282 | -0.5643 | 0.950521 | 0.012579 |
| 5 | 0.8169 | -0.2505 | 0.8435 | -0.2551 | -0.7949 | -0.2263 | 0.938346 | 0.015472 |
| 6 | 0.3702 | -0.2978 | 0.4483 | -0.3164 | -0.2572 | -0.2888 | 0.386752 | 0.014076 |
| 7 | 0.0213 | -0.2679 | -0.0719 | -0.2847 | -0.0370 | -0.2383 | 0.047087 | 0.023492 |
| 8 | -0.3784 | -0.2549 | -0.3327 | -0.2613 | 0.4308 | -0.2235 | 0.454574 | 0.020231 |
| 9 | -0.8672 | -0.2686 | -0.8469 | -0.2784 | 0.8573 | -0.2670 | 0.989832 | 0.006172 |
| 10 | 0.8101 | -0.0681 | 0.8329 | -0.0890 | -0.8119 | -0.0513 | 0.943113 | 0.018887 |
| 11 | 0.3269 | -0.0212 | 0.2945 | -0.0492 | -0.2557 | -0.0241 | 0.327412 | 0.015397 |
| 12 | 0.0000 | 0.0000 | 0.0000 | 0.0000 | 0.0000 | 0.0000 | 0 | 0 |
| 13 | -0.4392 | -0.0074 | -0.4231 | -0.0543 | 0.4939 | -0.0456 | 0.534139 | 0.024948 |
| 14 | -0.9168 | 0.0068 | -0.9010 | 0.0351 | 0.9433 | 0.0248 | 1.069397 | 0.014324 |

| | | | | | | | | |
|---|---|---|---|---|---|---|---|---|
| 15 | 0.8160 | 0.3759 | 0.8431 | 0.3443 | -0.8278 | 0.3771 | 0.956967 | 0.0186 |
| 16 | 0.3592 | 0.3855 | 0.3576 | 0.3553 | -0.3361 | 0.3537 | 0.400971 | 0.017916 |
| 17 | 0.0137 | 0.3432 | 0.0052 | 0.3182 | 0.0311 | 0.3210 | 0.013202 | 0.013697 |
| 18 | -0.4679 | 0.3541 | -0.4768 | 0.3607 | 0.4935 | 0.3721 | 0.557652 | 0.009106 |
| 19 | -0.8570 | 0.3584 | -0.8957 | 0.3558 | 0.9721 | 0.3957 | 1.067379 | 0.022324 |
| 20 | 0.8403 | 0.7071 | 0.8855 | 0.6902 | -0.8502 | 0.7265 | 0.989317 | 0.018164 |
| 21 | 0.3445 | 0.6877 | 0.3437 | 0.6420 | -0.3644 | 0.7103 | 0.409053 | 0.034795 |
| 22 | -0.0461 | 0.6410 | -0.0825 | 0.6327 | 0.1054 | 0.6847 | 0.099652 | 0.027936 |
| 23 | -0.4237 | 0.6629 | -0.4051 | 0.6646 | 0.4403 | 0.7038 | 0.493549 | 0.023138 |
| 24 | -0.7911 | 0.6716 | -0.8997 | 0.6586 | 0.9699 | 0.6970 | 1.04947 | 0.019531 |

## Comparison of Front Versus Back Surfaces

From the beginning, we were looking to see if we could get equivalent results by scanning the back of the heliostat. On many of the heliostats we have observed, the back side has the majority of the facet visible even with the support structure. These facets themselves are composed of a glass plate, with a mirror coating on the front side. To mount these plates to the heliostat structure, the NSTTF facets are cemented to a steel support structure that is then bolted to the heliostat frame. Figure 23 shows a photo of the back of an NSTTF heliostat. Figure 24 shows the back of another heliostat design from the Crescent Dunes Solar Facility in Tonopah, Nevada. These facets have a support frame fabricated directly onto the mirror. Both of these support structures can be seen in the point scan data, as shown in Figures 25 and Figure 26 respectively.

**Figure 23. Back of NSTTF heliostat**

**Figure 24. Back of Crescent Dunes heliostat**

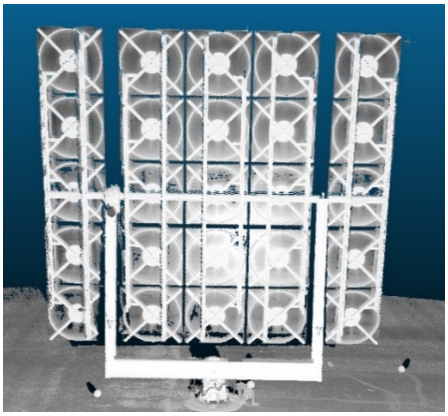

**Figure 25. LiDAR scan of back side, NSTTF**

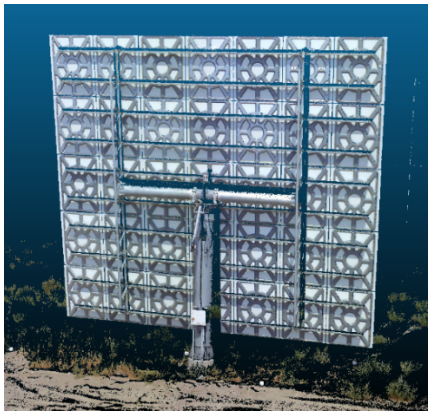

**Figure 26. LiDAR scan of back side, Crescent Dunes**

As seen in the images, a substantial portion of the facet is visible from the back. If this can be isolated, we should be able to use it to estimate the facet pointing direction. Unfortunately, the NSTTF back side is itself a reflective surface, and proved to be extremely noisy. However, the Crescent Dunes heliostat back side scanned very cleanly. Moreover, we were able to filter the data to remove the support structure, as shown in figure 27.

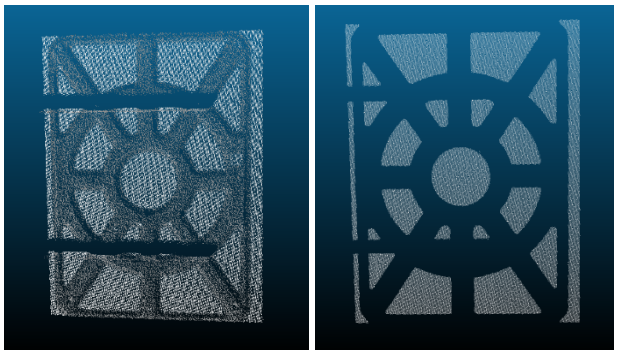

**Figure 27. Point cloud of facet, Crescent Dunes; a) segmented, b) support filtered out**

The hypothesis is the facet normal data should be the same for a front scan or a back scan. To test this, we registered scans from the front and back for the Crescent Dunes data. Registration refers to putting the scan data into a common coordinate frame. This was done using spherical scan targets that were placed around the heliostat for both scans. With the data in the same coordinate frame, the facet plane fitting is also in the same coordinate frame. The normals were expressed in azimuth and elevation as described above. Table 4 shows the comparison of the calculations. The results were very favorable, with the mean errors for the 35 facets at 0.0071 degrees for azimuth and 0.0003 degrees for elevation. The standard deviations values were 0.0562 degrees azimuth and 0.0465 degrees elevation.

**Table 4. Contrast of Azimuth and Elevation for front and back of same heliostat (Crescent Dunes 5903). (angles in degrees)**

| 5903_0_0_front | | | | 5903_0_0_back | | | | difference | difference |
|---|---|---|---|---|---|---|---|---|---|
| facet A | facet B | Azimuth | Elevation | facet A | facet B | Azimuth | Elevation | Az front-back | El front-back |
| 0 | 16 | -0.2543 | -0.2775 | 0 | 16 | -0.3923 | -0.2871 | 0.1380 | 0.0097 |
| 1 | 16 | -0.3407 | -0.3453 | 1 | 16 | -0.2318 | -0.3796 | -0.1089 | 0.0343 |
| 2 | 16 | -0.0397 | -0.4178 | 2 | 16 | -0.0314 | -0.4209 | -0.0083 | 0.0031 |
| 3 | 16 | -0.0157 | -0.4310 | 3 | 16 | -0.0127 | -0.4299 | -0.0030 | -0.0010 |
| 4 | 16 | 0.0076 | -0.4257 | 4 | 16 | 0.0192 | -0.3992 | -0.0116 | -0.0265 |
| 5 | 16 | 0.0943 | -0.4191 | 5 | 16 | 0.1213 | -0.3729 | -0.0269 | -0.0461 |
| 6 | 16 | 0.3043 | -0.2825 | 6 | 16 | 0.2518 | -0.3167 | 0.0525 | 0.0343 |
| 7 | 16 | -0.3086 | -0.1428 | 7 | 16 | -0.4595 | -0.1544 | 0.1509 | 0.0116 |
| 8 | 16 | -0.2984 | -0.1573 | 8 | 16 | -0.2161 | -0.1705 | -0.0823 | 0.0131 |
| 9 | 16 | -0.0328 | -0.2253 | 9 | 16 | -0.0264 | -0.2193 | -0.0064 | -0.0060 |
| 10 | 16 | -0.0242 | -0.2394 | 10 | 16 | -0.0130 | -0.2424 | -0.0112 | 0.0030 |
| 11 | 16 | -0.0207 | -0.2510 | 11 | 16 | -0.0344 | -0.2419 | 0.0138 | -0.0092 |
| 12 | 16 | 0.1537 | -0.2385 | 12 | 16 | 0.1658 | -0.2001 | -0.0121 | -0.0384 |
| 13 | 16 | 0.3468 | -0.1615 | 13 | 16 | 0.3133 | -0.1978 | 0.0335 | 0.0362 |
| 14 | 16 | -0.2029 | -0.4331 | 14 | 16 | -0.2922 | -0.3863 | 0.0893 | -0.0468 |
| 15 | 16 | -0.1434 | -0.1444 | 15 | 16 | -0.0932 | -0.1962 | -0.0502 | 0.0518 |
| 16 | 16 | 0.0000 | 0.0000 | 16 | 16 | 0.0000 | 0.0000 | 0.0000 | 0.0000 |
| 17 | 16 | -0.0331 | 0.0775 | 17 | 16 | -0.0216 | 0.1075 | -0.0114 | -0.0301 |
| 18 | 16 | -0.0583 | -0.0013 | 18 | 16 | -0.0548 | -0.0045 | -0.0035 | 0.0032 |
| 19 | 16 | 0.0117 | -0.1988 | 19 | 16 | 0.0194 | -0.1961 | -0.0077 | -0.0027 |
| 20 | 16 | 0.2069 | -0.3641 | 20 | 16 | 0.1743 | -0.3845 | 0.0326 | 0.0204 |

| | | | | | | | | | | |
|---|---|---|---|---|---|---|---|---|---|---|
| 21 | 16 | -0.1804 | 0.1181 | 21 | 16 | -0.2936 | 0.0752 | | 0.1132 | 0.0429 |
| 22 | 16 | -0.1577 | -0.0200 | 22 | 16 | -0.1370 | -0.0051 | | -0.0206 | -0.0149 |
| 23 | 16 | 0.0660 | 0.0155 | 23 | 16 | 0.0583 | -0.0326 | | 0.0077 | 0.0481 |
| 24 | 16 | -0.0218 | 0.0221 | 24 | 16 | -0.0391 | -0.0067 | | 0.0173 | 0.0287 |
| 25 | 16 | -0.0798 | -0.0150 | 25 | 16 | -0.1010 | -0.0347 | | 0.0212 | 0.0198 |
| 26 | 16 | 0.0629 | 0.0278 | 26 | 16 | 0.1238 | -0.0182 | | -0.0609 | 0.0460 |
| 27 | 16 | 0.0020 | -0.0593 | 27 | 16 | -0.0463 | -0.0714 | | 0.0482 | 0.0121 |
| 28 | 16 | -0.3257 | 0.0266 | 28 | 16 | -0.2711 | 0.0249 | | -0.0546 | 0.0017 |
| 29 | 16 | -0.1500 | 0.0224 | 29 | 16 | -0.1860 | -0.0004 | | 0.0361 | 0.0228 |
| 30 | 16 | -0.0365 | -0.0270 | 30 | 16 | 0.0146 | -0.0358 | | -0.0512 | 0.0088 |
| 31 | 16 | -0.0336 | -0.2368 | 31 | 16 | -0.0430 | -0.0205 | | 0.0094 | -0.2163 |
| 32 | 16 | -0.0070 | -0.0465 | 32 | 16 | -0.0575 | 0.0037 | | 0.0506 | -0.0502 |
| 33 | 16 | 0.1043 | 0.0496 | 33 | 16 | 0.1481 | 0.0301 | | -0.0439 | 0.0195 |
| 34 | 16 | -0.1730 | 0.0840 | 34 | 16 | -0.1806 | 0.0555 | | 0.0076 | 0.0285 |
| | | | | | | | | mean | 0.0071 | 0.0003 |
| | | | | | | | | stddev | 0.0562 | 0.0465 |

## COMPARE AND CONTRAST THE ACCURACY OF THE SCAN TO OTHER METHODS.

As referenced in the **Introduction**, Sandia has a concurrent project called Universal Field Assessment, Correction, and Enhancement Tool (UFACET) that uses another optical technique to measure facet canting angles. This method uses a camera to capture the reflectance of known geometry in the heliostat facet mirrors, and then calculates the shape and angle of the facets by comparing the relationship of the ideal to the actual reflectance image. The paper sited shows comparative data from both techniques [3]. The RMS difference in the canting error estimates between the UFACET method and the LiDAR system on a NSTTF heliostat with 25 facets was around 0.8 mrad for both azimuth and elevation directions.

## ASSESS LIDAR METHOD FOR REPEATABILITY AND ACCURACY.

A repeatability study was performed at the NSTTF which acquired more than 230 individual scans of 13 heliostats at 3 different elevation angles. Each heliostat was scanned at 3 or 4 different heliostat elevation angles; 0 degrees (vertical), 25 degrees, 30 degrees and 45 degrees. We scanned multiple (5 → 9) times at each discrete elevation angle. We then derived the relative canting angles for each scan. The standard deviation of the derived azimuth and elevation angle was calculated for each individual facet within that set of scans. We then took the RMS error of the standard deviations for each heliostat, yielding 40 discrete RMS errors in azimuth and elevation. The average RMS error in Azimuth was 0.21 mrad, and the average RMS error of Elevation was 0.20 mrad.

The processed data is presented over the next 4 pages in Tables 5 and 6. Each cell is the standard deviation (from 5-9 individual scans) of the difference between that facet's angle relative to the center facet, with Table 5 showing the azimuth and Table 6 showing the elevation. Each row represents between 5 and 9 scans for a heliostat/elevation angle pair.

**Table 5. Standard Deviation of facet azimuth angles (relative to center facet) per heliostat elevation angle pair**

| HS-Elev | 0 | 1 | 2 | 3 | 4 | 5 | 6 | 7 | 8 | 9 | 10 | 11 | 12 | 13 | 14 | 15 | 16 | 17 | 18 | 19 | 20 | 21 | 22 | 23 | 24 | AZ-rms |
|---|---|---|---|---|---|---|---|---|---|---|---|---|---|---|---|---|---|---|---|---|---|---|---|---|---|---|
| 12E14-45 | 0.15 | 0.10 | 0.07 | 0.13 | 0.16 | 0.11 | 0.08 | 0.10 | 0.12 | 0.08 | 0.04 | 0.10 | 0.00 | 0.16 | 0.18 | 0.10 | 0.12 | 0.05 | 0.14 | 0.20 | 0.11 | 0.10 | 0.05 | 0.15 | 0.19 | **0.12** |
| 12E14-0 | 0.12 | 0.24 | 0.15 | 0.24 | 0.35 | 0.10 | 0.13 | 0.07 | 0.22 | 0.28 | 0.09 | 0.23 | 0.00 | 0.18 | 0.27 | 0.08 | 0.10 | 0.06 | 0.18 | 0.16 | 0.24 | 0.18 | 0.05 | 0.09 | 0.10 | **0.18** |
| 12E14-30 | 0.15 | 0.17 | 0.09 | 0.23 | 0.10 | 0.15 | 0.19 | 0.20 | 0.21 | 0.13 | 0.09 | 0.20 | 0.00 | 0.25 | 0.35 | 0.20 | 0.17 | 0.15 | 0.18 | 0.11 | 0.22 | 0.17 | 0.12 | 0.16 | 0.17 | **0.18** |
| 12E14-25 | 0.17 | 0.13 | 0.07 | 0.13 | 0.32 | 0.08 | 0.15 | 0.10 | 0.13 | 0.28 | 0.06 | 0.11 | 0.00 | 0.13 | 0.37 | 0.20 | 0.12 | 0.08 | 0.08 | 0.28 | 0.14 | 0.12 | 0.08 | 0.06 | 0.27 | **0.17** |
| 09W08-45 | 0.18 | 0.14 | 0.19 | 0.14 | 0.11 | 0.21 | 0.13 | 0.13 | 0.12 | 0.09 | 0.09 | 0.17 | 0.00 | 0.14 | 0.08 | 0.06 | 0.08 | 0.12 | 0.13 | 0.12 | 0.13 | 0.10 | 0.07 | 0.05 | 0.09 | **0.12** |
| 09W01-45 | 0.26 | 0.41 | 0.27 | 0.20 | 0.27 | 0.10 | 0.32 | 0.13 | 0.11 | 0.15 | 0.07 | 0.14 | 0.00 | 0.03 | 0.05 | 0.19 | 0.18 | 0.12 | 0.16 | 0.16 | 0.32 | 0.28 | 0.27 | 0.29 | 0.31 | **0.22** |
| 09W01-30 | 0.20 | 0.33 | 0.06 | 0.12 | 0.17 | 0.20 | 0.35 | 0.06 | 0.14 | 0.16 | 0.21 | 0.12 | 0.00 | 0.14 | 0.14 | 0.21 | 0.40 | 0.05 | 0.11 | 0.13 | 0.07 | 0.19 | 0.11 | 0.13 | 0.15 | **0.18** |
| 09W01-25 | 0.54 | 0.38 | 0.08 | 0.26 | 0.12 | 0.36 | 0.26 | 0.06 | 0.22 | 0.12 | 0.31 | 0.46 | 0.00 | 0.18 | 0.13 | 0.33 | 0.19 | 0.08 | 0.15 | 0.14 | 0.34 | 0.26 | 0.16 | 0.13 | 0.16 | **0.25** |
| 08W08-30 | 0.23 | 0.32 | 0.24 | 0.25 | 0.17 | 0.15 | 0.17 | 0.22 | 0.23 | 0.20 | 0.10 | 0.27 | 0.00 | 0.18 | 0.17 | 0.08 | 0.14 | 0.11 | 0.17 | 0.15 | 0.08 | 0.15 | 0.14 | 0.15 | 0.15 | **0.18** |
| 08W08-25 | 0.16 | 0.27 | 0.19 | 0.25 | 0.24 | 0.24 | 0.22 | 0.22 | 0.18 | 0.16 | 0.09 | 0.18 | 0.00 | 0.18 | 0.13 | 0.11 | 0.06 | 0.23 | 0.15 | 0.12 | 0.19 | 0.12 | 0.17 | 0.12 | 0.26 | **0.18** |
| 08W07-45 | 0.24 | 0.22 | 0.15 | 0.09 | 0.14 | 0.13 | 0.14 | 0.11 | 0.07 | 0.17 | 0.19 | 0.12 | 0.00 | 0.16 | 0.10 | 0.11 | 0.21 | 0.06 | 0.10 | 0.17 | 0.08 | 0.17 | 0.18 | 0.16 | 0.10 | **0.14** |
| 08W07-30 | 0.36 | 0.18 | 0.22 | 0.16 | 0.08 | 0.31 | 0.27 | 0.14 | 0.08 | 0.11 | 0.23 | 0.31 | 0.00 | 0.04 | 0.10 | 0.16 | 0.26 | 0.11 | 0.09 | 0.15 | 0.26 | 0.12 | 0.07 | 0.13 | 0.10 | **0.18** |
| 08W07-25 | 0.32 | 0.23 | 0.23 | 0.24 | 0.23 | 0.08 | 0.12 | 0.20 | 0.24 | 0.33 | 0.28 | 0.32 | 0.00 | 0.07 | 0.22 | 0.13 | 0.19 | 0.08 | 0.17 | 0.23 | 0.39 | 0.53 | 0.25 | 0.15 | 0.15 | **0.24** |
| 08W06-45 | 0.13 | 0.16 | 0.11 | 0.11 | 0.13 | 0.12 | 0.21 | 0.15 | 0.16 | 0.13 | 0.15 | 0.15 | 0.00 | 0.10 | 0.10 | 0.12 | 0.13 | 0.13 | 0.17 | 0.11 | 0.28 | 0.14 | 0.17 | 0.11 | 0.17 | **0.15** |
| 08W06-30 | 0.13 | 0.30 | 0.17 | 0.20 | 0.24 | 0.09 | 0.21 | 0.11 | 0.21 | 0.26 | 0.10 | 0.12 | 0.00 | 0.12 | 0.21 | 0.19 | 0.11 | 0.15 | 0.16 | 0.15 | 0.21 | 0.20 | 0.12 | 0.20 | 0.09 | **0.17** |
| 08W06-25 | 0.32 | 1.22 | 0.38 | 0.56 | 0.18 | 0.34 | 0.69 | 0.23 | 0.49 | 0.17 | 0.48 | 0.36 | 0.00 | 0.32 | 0.18 | 0.51 | 0.33 | 0.13 | 0.15 | 0.14 | 0.46 | 0.31 | 0.10 | 0.12 | 0.12 | **0.41** |
| 07W08-45 | 0.63 | 0.84 | 0.43 | 0.72 | 0.12 | 0.35 | 0.82 | 0.31 | 0.69 | 0.11 | 0.56 | 0.74 | 0.00 | 0.57 | 0.34 | 0.57 | 0.87 | 0.15 | 0.48 | 0.47 | 0.18 | 0.47 | 0.22 | 0.46 | 0.57 | **0.53** |
| 07W08-30 | 0.07 | 0.20 | 0.22 | 0.18 | 0.23 | 0.17 | 0.47 | 0.27 | 0.24 | 0.18 | 0.19 | 0.37 | 0.00 | 0.20 | 0.29 | 0.14 | 0.10 | 0.18 | 0.15 | 0.15 | 0.08 | 0.18 | 0.18 | 0.23 | 0.13 | **0.21** |
| 07W08-25 | 0.21 | 0.45 | 0.14 | 0.16 | 0.18 | 0.18 | 0.17 | 0.06 | 0.22 | 0.17 | 0.18 | 0.29 | 0.00 | 0.15 | 0.17 | 0.12 | 0.43 | 0.16 | 0.15 | 0.17 | 0.10 | 0.22 | 0.19 | 0.16 | 0.15 | **0.21** |

**Table 5.** (continued)

| HS-Elev | 0 | 1 | 2 | 3 | 4 | 5 | 6 | 7 | 8 | 9 | 10 | 11 | 12 | 13 | 14 | 15 | 16 | 17 | 18 | 19 | 20 | 21 | 22 | 23 | 24 | AZ-rms |
|---|---|---|---|---|---|---|---|---|---|---|---|---|---|---|---|---|---|---|---|---|---|---|---|---|---|---|
| 07W07-30 | 0.17 | 0.25 | 0.09 | 0.14 | 0.22 | 0.15 | 0.27 | 0.12 | 0.18 | 0.25 | 0.19 | 0.28 | 0.00 | 0.21 | 0.12 | 0.13 | 0.15 | 0.16 | 0.26 | 0.18 | 0.08 | 0.10 | 0.14 | 0.24 | 0.15 | **0.18** |
| 07W07-25 | 0.21 | 0.32 | 0.16 | 0.22 | 0.22 | 0.23 | 0.29 | 0.18 | 0.19 | 0.17 | 0.11 | 0.20 | 0.00 | 0.36 | 0.11 | 0.13 | 0.25 | 0.13 | 0.07 | 0.17 | 0.15 | 0.39 | 0.06 | 0.17 | 0.24 | **0.21** |
| 07W07-45 | 0.25 | 0.34 | 0.28 | 0.08 | 0.22 | 0.09 | 0.29 | 0.08 | 0.14 | 0.17 | 0.10 | 0.20 | 0.00 | 0.16 | 0.19 | 0.10 | 0.12 | 0.08 | 0.06 | 0.08 | 0.10 | 0.06 | 0.09 | 0.06 | 0.08 | **0.16** |
| 07W06-45 | 0.28 | 0.18 | 0.17 | 0.08 | 0.15 | 0.12 | 0.11 | 0.16 | 0.08 | 0.11 | 0.26 | 0.12 | 0.00 | 0.17 | 0.11 | 0.16 | 0.15 | 0.08 | 0.12 | 0.23 | 0.20 | 0.15 | 0.17 | 0.22 | 0.18 | **0.16** |
| 07W06-30 | 0.16 | 0.19 | 0.05 | 0.12 | 0.13 | 0.05 | 0.09 | 0.07 | 0.09 | 0.09 | 0.15 | 0.16 | 0.00 | 0.08 | 0.13 | 0.09 | 0.10 | 0.09 | 0.05 | 0.09 | 0.21 | 0.04 | 0.12 | 0.11 | 0.12 | **0.11** |
| 07W06-25 | 0.34 | 0.44 | 0.15 | 0.31 | 0.37 | 0.23 | 0.23 | 0.10 | 0.22 | 0.31 | 0.30 | 0.24 | 0.00 | 0.22 | 0.29 | 0.44 | 0.20 | 0.12 | 0.14 | 0.14 | 0.17 | 0.15 | 0.22 | 0.18 | 0.17 | **0.25** |
| 06W08-30 | 0.20 | 0.27 | 0.22 | 0.32 | 0.14 | 0.16 | 0.25 | 0.14 | 0.29 | 0.13 | 0.19 | 0.24 | 0.00 | 0.30 | 0.15 | 0.09 | 0.19 | 0.17 | 0.10 | 0.18 | 0.27 | 0.23 | 0.19 | 0.09 | 0.25 | **0.20** |
| 06W08-25 | 0.15 | 0.19 | 0.20 | 0.18 | 0.19 | 0.15 | 0.14 | 0.22 | 0.16 | 0.06 | 0.19 | 0.09 | 0.00 | 0.21 | 0.22 | 0.19 | 0.27 | 0.12 | 0.07 | 0.24 | 0.15 | 0.26 | 0.22 | 0.16 | 0.20 | **0.18** |
| 06W08-45 | 0.11 | 0.19 | 0.19 | 0.21 | 0.72 | 0.22 | 0.16 | 0.20 | 0.17 | 0.92 | 0.29 | 0.10 | 0.00 | 0.30 | 1.10 | 0.21 | 0.17 | 0.16 | 0.14 | 0.68 | 0.20 | 0.15 | 0.21 | 0.12 | 0.60 | **0.40** |
| 06W07-30 | 0.75 | 0.27 | 0.16 | 0.29 | 0.53 | 0.60 | 0.13 | 0.13 | 0.27 | 0.61 | 0.40 | 0.22 | 0.00 | 0.20 | 0.56 | 0.29 | 0.23 | 0.14 | 0.22 | 0.68 | 0.12 | 0.48 | 0.18 | 0.21 | 0.50 | **0.38** |
| 06W07-25 | 0.29 | 0.18 | 0.23 | 0.26 | 0.24 | 0.29 | 0.18 | 0.21 | 0.30 | 0.08 | 0.18 | 0.35 | 0.00 | 0.33 | 0.54 | 0.22 | 0.34 | 0.20 | 0.08 | 0.32 | 0.25 | 0.19 | 0.19 | 0.20 | 0.17 | **0.26** |
| 06W07-45 | 0.20 | 0.33 | 0.13 | 0.14 | 0.05 | 0.17 | 0.12 | 0.22 | 0.13 | 0.19 | 0.11 | 0.23 | 0.00 | 0.13 | 0.13 | 0.16 | 0.16 | 0.13 | 0.26 | 0.21 | 0.12 | 0.10 | 0.14 | 0.11 | 0.12 | **0.16** |
| 06W06-30 | 0.23 | 0.25 | 0.04 | 0.55 | 0.19 | 0.13 | 0.21 | 0.06 | 0.36 | 0.27 | 0.23 | 0.21 | 0.00 | 0.36 | 0.20 | 0.26 | 0.12 | 0.21 | 0.16 | 0.20 | 0.23 | 0.20 | 0.33 | 0.18 | 0.19 | **0.24** |
| 06W06-25 | 0.25 | 0.22 | 0.27 | 0.32 | 0.46 | 0.24 | 0.21 | 0.13 | 0.25 | 0.20 | 0.38 | 0.23 | 0.00 | 0.27 | 0.66 | 0.18 | 0.28 | 0.14 | 0.07 | 0.14 | 0.25 | 0.23 | 0.14 | 0.13 | 0.14 | **0.27** |
| 06W06-45 | 0.16 | 0.24 | 0.30 | 0.08 | 0.14 | 0.18 | 0.14 | 0.18 | 0.24 | 0.15 | 0.13 | 0.10 | 0.00 | 0.59 | 0.19 | 0.05 | 0.09 | 0.21 | 0.36 | 0.07 | 0.24 | 0.10 | 0.10 | 0.25 | 0.20 | **0.21** |
| 05W05-45 | 0.35 | 0.25 | 0.25 | 0.15 | 0.43 | 0.17 | 0.24 | 0.23 | 0.28 | 0.25 | 0.27 | 0.24 | 0.00 | 0.11 | 0.23 | 0.21 | 0.24 | 0.26 | 0.10 | 0.13 | 0.28 | 0.29 | 0.25 | 0.19 | 0.21 | **0.24** |
| 05W05-0 | 0.10 | 0.21 | 0.07 | 0.11 | 0.05 | 0.06 | 0.12 | 0.14 | 0.11 | 0.09 | 0.03 | 0.08 | 0.00 | 0.11 | 0.09 | 0.06 | 0.05 | 0.07 | 0.09 | 0.07 | 0.12 | 0.11 | 0.12 | 0.12 | 0.10 | **0.10** |
| 05W05-45 | 0.35 | 0.25 | 0.25 | 0.15 | 0.43 | 0.17 | 0.24 | 0.23 | 0.28 | 0.25 | 0.27 | 0.24 | 0.00 | 0.11 | 0.23 | 0.21 | 0.24 | 0.26 | 0.10 | 0.13 | 0.28 | 0.29 | 0.25 | 0.19 | 0.21 | **0.24** |
| 05W05-25 | 0.19 | 0.32 | 0.34 | 0.47 | 0.36 | 0.25 | 0.32 | 0.48 | 0.31 | 0.36 | 0.44 | 0.44 | 0.00 | 0.44 | 0.46 | 0.41 | 0.44 | 0.27 | 0.52 | 0.35 | 0.28 | 0.41 | 0.32 | 0.33 | 0.38 | **0.37** |
| 05W03-45 | 0.14 | 0.24 | 0.11 | 0.13 | 0.30 | 0.22 | 0.11 | 0.17 | 0.10 | 0.09 | 0.12 | 0.07 | 0.00 | 0.08 | 0.13 | 0.18 | 0.12 | 0.08 | 0.14 | 0.11 | 0.09 | 0.19 | 0.12 | 0.12 | 0.09 | **0.14** |
| 05W03-25 | 0.25 | 0.16 | 0.08 | 0.13 | 0.07 | 0.14 | 0.08 | 0.08 | 0.09 | 0.08 | 0.12 | 0.06 | 0.00 | 0.06 | 0.14 | 0.05 | 0.09 | 0.06 | 0.12 | 0.12 | 0.06 | 0.16 | 0.05 | 0.12 | 0.15 | **0.11** |
| 05W03-0 | 0.16 | 0.07 | 0.15 | 0.36 | 0.16 | 0.17 | 0.19 | 0.12 | 0.29 | 0.15 | 0.07 | 0.11 | 0.00 | 0.19 | 0.11 | 0.13 | 0.11 | 0.13 | 0.10 | 0.11 | 0.08 | 0.38 | 0.24 | 0.08 | 0.08 | **0.17** |
| **Avg** | **0.24** | **0.28** | **0.18** | **0.22** | **0.23** | **0.19** | **0.23** | **0.16** | **0.21** | **0.20** | **0.20** | **0.22** | **0.00** | **0.20** | **0.24** | **0.18** | **0.20** | **0.13** | **0.16** | **0.19** | **0.19** | **0.21** | **0.16** | **0.16** | **0.19** | 0.21 |

**Table 6. Standard Deviation of facet elevation angles (relative to center facet) per heliostat elevation angle pair**

| HS-Elev | 0 | 1 | 2 | 3 | 4 | 5 | 6 | 7 | 8 | 9 | 10 | 11 | 12 | 13 | 14 | 15 | 16 | 17 | 18 | 19 | 20 | 21 | 22 | 23 | 24 | EL-rms |
|---|---|---|---|---|---|---|---|---|---|---|---|---|---|---|---|---|---|---|---|---|---|---|---|---|---|---|
| 12E14-45 | 0.18 | 0.28 | 0.12 | 0.22 | 0.17 | 0.24 | 0.20 | 0.20 | 0.10 | 0.22 | 0.28 | 0.17 | 0.00 | 0.14 | 0.34 | 0.14 | 0.14 | 0.06 | 0.15 | 0.17 | 0.12 | 0.21 | 0.10 | 0.25 | 0.12 | **0.19** |
| 12E14-0 | 0.05 | 0.18 | 0.09 | 0.10 | 0.10 | 0.04 | 0.08 | 0.08 | 0.09 | 0.14 | 0.06 | 0.10 | 0.00 | 0.09 | 0.06 | 0.09 | 0.09 | 0.12 | 0.07 | 0.06 | 0.39 | 0.55 | 0.15 | 0.16 | 0.09 | **0.17** |
| 12E14-30 | 0.16 | 0.20 | 0.13 | 0.19 | 0.12 | 0.09 | 0.17 | 0.13 | 0.13 | 0.22 | 0.14 | 0.19 | 0.00 | 0.17 | 0.17 | 0.16 | 0.09 | 0.09 | 0.15 | 0.07 | 0.12 | 0.18 | 0.18 | 0.14 | 0.23 | **0.15** |
| 12E14-25 | 0.10 | 0.14 | 0.13 | 0.16 | 0.15 | 0.15 | 0.10 | 0.16 | 0.18 | 0.12 | 0.16 | 0.08 | 0.00 | 0.04 | 0.16 | 0.09 | 0.07 | 0.09 | 0.16 | 0.12 | 0.20 | 0.08 | 0.11 | 0.15 | 0.05 | **0.13** |
| 09W08-45 | 0.07 | 0.09 | 0.10 | 0.08 | 0.05 | 0.11 | 0.16 | 0.11 | 0.11 | 0.08 | 0.08 | 0.07 | 0.00 | 0.08 | 0.06 | 0.12 | 0.09 | 0.09 | 0.05 | 0.09 | 0.08 | 0.04 | 0.09 | 0.06 | 0.10 | **0.09** |
| 09W01-45 | 0.35 | 0.16 | 0.19 | 0.18 | 0.30 | 0.34 | 0.11 | 0.09 | 0.11 | 0.28 | 0.34 | 0.15 | 0.00 | 0.17 | 0.28 | 0.34 | 0.17 | 0.08 | 0.09 | 0.32 | 0.36 | 0.18 | 0.06 | 0.14 | 0.31 | **0.23** |
| 09W01-30 | 0.06 | 0.10 | 0.05 | 0.11 | 0.10 | 0.09 | 0.13 | 0.05 | 0.05 | 0.10 | 0.12 | 0.08 | 0.00 | 0.08 | 0.08 | 0.14 | 0.07 | 0.05 | 0.07 | 0.09 | 0.10 | 0.11 | 0.04 | 0.12 | 0.13 | **0.09** |
| 09W01-25 | 0.11 | 0.11 | 0.02 | 0.05 | 0.04 | 0.07 | 0.05 | 0.03 | 0.04 | 0.04 | 0.06 | 0.06 | 0.00 | 0.02 | 0.03 | 0.08 | 0.05 | 0.03 | 0.01 | 0.02 | 0.09 | 0.06 | 0.04 | 0.05 | 0.05 | **0.06** |
| 08W08-30 | 0.02 | 0.08 | 0.14 | 0.06 | 0.09 | 0.10 | 0.20 | 0.08 | 0.23 | 0.14 | 0.12 | 0.11 | 0.00 | 0.10 | 0.08 | 0.11 | 0.11 | 0.10 | 0.07 | 0.05 | 0.10 | 0.11 | 0.07 | 0.09 | 0.11 | **0.11** |
| 08W08-25 | 0.21 | 0.28 | 0.22 | 0.16 | 0.35 | 0.27 | 0.18 | 0.29 | 0.28 | 0.21 | 0.25 | 0.18 | 0.00 | 0.12 | 0.21 | 0.12 | 0.10 | 0.22 | 0.16 | 0.23 | 0.20 | 0.15 | 0.30 | 0.21 | 0.26 | **0.22** |
| 08W07-45 | 0.42 | 0.40 | 0.23 | 0.28 | 0.33 | 0.40 | 0.64 | 0.26 | 0.27 | 0.37 | 0.35 | 0.29 | 0.00 | 0.27 | 0.31 | 0.41 | 0.34 | 0.39 | 0.41 | 0.38 | 0.29 | 0.25 | 0.27 | 0.34 | 0.29 | **0.34** |
| 08W07-30 | 0.20 | 0.14 | 0.16 | 0.15 | 0.13 | 0.16 | 0.24 | 0.12 | 0.17 | 0.19 | 0.15 | 0.14 | 0.00 | 0.14 | 0.10 | 0.18 | 0.19 | 0.22 | 0.16 | 0.10 | 0.23 | 0.17 | 0.12 | 0.19 | 0.15 | **0.16** |
| 08W07-25 | 0.19 | 0.70 | 0.60 | 0.48 | 0.56 | 0.16 | 0.26 | 0.58 | 0.48 | 0.36 | 0.14 | 0.22 | 0.00 | 0.18 | 0.16 | 0.50 | 0.24 | 0.14 | 0.23 | 0.19 | 0.22 | 0.33 | 0.36 | 0.26 | 0.45 | **0.36** |
| 08W06-45 | 0.30 | 0.19 | 0.19 | 0.19 | 0.26 | 0.30 | 0.19 | 0.36 | 0.29 | 0.31 | 0.40 | 0.24 | 0.00 | 0.20 | 0.36 | 0.46 | 0.25 | 0.19 | 0.21 | 0.43 | 0.53 | 0.31 | 0.25 | 0.30 | 0.62 | **0.32** |
| 08W06-30 | 0.06 | 0.07 | 0.13 | 0.15 | 0.13 | 0.06 | 0.12 | 0.14 | 0.10 | 0.14 | 0.13 | 0.13 | 0.00 | 0.15 | 0.08 | 0.13 | 0.12 | 0.14 | 0.13 | 0.11 | 0.09 | 0.08 | 0.09 | 0.07 | 0.07 | **0.11** |
| 08W06-25 | 0.07 | 0.08 | 0.09 | 0.10 | 0.11 | 0.11 | 0.10 | 0.06 | 0.06 | 0.09 | 0.16 | 0.11 | 0.00 | 0.14 | 0.11 | 0.14 | 0.15 | 0.09 | 0.04 | 0.10 | 0.17 | 0.09 | 0.09 | 0.08 | 0.07 | **0.10** |
| 07W08-45 | 0.14 | 0.19 | 0.08 | 0.16 | 0.15 | 0.20 | 0.18 | 0.15 | 0.14 | 0.17 | 0.21 | 0.10 | 0.00 | 0.05 | 0.18 | 0.19 | 0.13 | 0.14 | 0.07 | 0.14 | 0.17 | 0.13 | 0.12 | 0.09 | 0.14 | **0.15** |
| 07W08-30 | 0.14 | 0.18 | 0.53 | 0.24 | 0.29 | 0.28 | 0.28 | 0.21 | 0.17 | 0.28 | 0.18 | 0.37 | 0.00 | 0.18 | 0.25 | 0.28 | 0.12 | 0.23 | 0.16 | 0.25 | 0.12 | 0.30 | 0.17 | 0.15 | 0.28 | **0.25** |
| 07W08-25 | 0.11 | 0.06 | 0.10 | 0.14 | 0.16 | 0.15 | 0.10 | 0.10 | 0.15 | 0.15 | 0.15 | 0.10 | 0.00 | 0.07 | 0.25 | 0.09 | 0.16 | 0.17 | 0.14 | 0.15 | 0.07 | 0.08 | 0.15 | 0.07 | 0.13 | **0.13** |

**Table 6.** (continued)

| HS-Elev | 0 | 1 | 2 | 3 | 4 | 5 | 6 | 7 | 8 | 9 | 10 | 11 | 12 | 13 | 14 | 15 | 16 | 17 | 18 | 19 | 20 | 21 | 22 | 23 | 24 | EL-rms |
|---|---|---|---|---|---|---|---|---|---|---|---|---|---|---|---|---|---|---|---|---|---|---|---|---|---|---|
| 07W07-30 | 0.04 | 0.07 | 0.08 | 0.09 | 0.16 | 0.08 | 0.15 | 0.07 | 0.12 | 0.11 | 0.05 | 0.13 | 0.00 | 0.17 | 0.07 | 0.13 | 0.11 | 0.06 | 0.13 | 0.09 | 0.11 | 0.11 | 0.07 | 0.09 | 0.05 | **0.10** |
| 07W07-25 | 0.31 | 0.06 | 0.07 | 0.06 | 0.15 | 0.21 | 0.09 | 0.08 | 0.07 | 0.16 | 0.17 | 0.08 | 0.00 | 0.16 | 0.13 | 0.17 | 0.10 | 0.11 | 0.08 | 0.06 | 0.12 | 0.09 | 0.12 | 0.10 | 0.12 | **0.13** |
| 07W07-45 | 0.37 | 0.21 | 0.18 | 0.03 | 0.37 | 0.22 | 0.07 | 0.14 | 0.16 | 0.14 | 0.17 | 0.15 | 0.00 | 0.16 | 0.23 | 0.09 | 0.13 | 0.10 | 0.20 | 0.23 | 0.15 | 0.14 | 0.12 | 0.14 | 0.16 | **0.18** |
| 07W06-45 | 0.61 | 0.22 | 0.19 | 0.22 | 0.52 | 0.46 | 0.25 | 0.23 | 0.29 | 0.26 | 0.31 | 0.20 | 0.00 | 0.31 | 0.38 | 0.28 | 0.30 | 0.17 | 0.39 | 0.19 | 0.39 | 0.39 | 0.38 | 0.25 | 0.40 | **0.33** |
| 07W06-30 | 0.08 | 0.11 | 0.13 | 0.10 | 0.09 | 0.11 | 0.14 | 0.15 | 0.08 | 0.17 | 0.07 | 0.17 | 0.00 | 0.14 | 0.10 | 0.13 | 0.09 | 0.06 | 0.17 | 0.10 | 0.14 | 0.08 | 0.06 | 0.08 | 0.07 | **0.11** |
| 07W06-25 | 0.22 | 0.14 | 0.10 | 0.14 | 0.18 | 0.14 | 0.19 | 0.17 | 0.20 | 0.12 | 0.16 | 0.24 | 0.00 | 0.18 | 0.24 | 0.18 | 0.09 | 0.17 | 0.14 | 0.14 | 0.14 | 0.14 | 0.13 | 0.14 | 0.15 | **0.16** |
| 06W08-30 | 0.19 | 0.13 | 0.07 | 0.17 | 0.31 | 0.07 | 0.20 | 0.14 | 0.10 | 0.18 | 0.17 | 0.07 | 0.00 | 0.26 | 0.14 | 0.15 | 0.05 | 0.12 | 0.11 | 0.25 | 0.07 | 0.09 | 0.03 | 0.18 | 0.10 | **0.15** |
| 06W08-25 | 0.17 | 0.14 | 0.12 | 0.11 | 0.15 | 0.19 | 0.15 | 0.14 | 0.12 | 0.09 | 0.18 | 0.13 | 0.00 | 0.15 | 0.14 | 0.18 | 0.17 | 0.16 | 0.18 | 0.08 | 0.17 | 0.07 | 0.11 | 0.12 | 0.13 | **0.14** |
| 06W08-45 | 0.17 | 0.38 | 0.27 | 0.25 | 0.67 | 0.19 | 0.19 | 0.15 | 0.35 | 0.20 | 0.24 | 0.18 | 0.00 | 0.33 | 0.25 | 0.28 | 0.34 | 0.19 | 0.37 | 0.59 | 0.27 | 0.09 | 0.10 | 0.18 | 0.20 | **0.29** |
| 06W07-30 | 0.30 | 0.09 | 0.25 | 0.14 | 0.25 | 0.12 | 0.20 | 0.12 | 0.17 | 0.18 | 0.18 | 0.13 | 0.00 | 0.34 | 0.10 | 0.08 | 0.18 | 0.21 | 0.16 | 0.19 | 0.12 | 0.25 | 0.17 | 0.21 | 0.18 | **0.19** |
| 06W07-25 | 0.34 | 0.26 | 0.16 | 0.18 | 0.23 | 0.15 | 0.15 | 0.08 | 0.06 | 0.08 | 0.32 | 0.21 | 0.00 | 0.63 | 0.41 | 0.18 | 0.25 | 0.21 | 0.39 | 0.53 | 0.13 | 0.16 | 0.10 | 0.17 | 0.41 | **0.28** |
| 06W07-45 | 0.41 | 0.18 | 0.25 | 0.42 | 0.32 | 0.19 | 0.17 | 0.21 | 0.09 | 0.16 | 0.21 | 0.15 | 0.00 | 0.17 | 0.13 | 0.13 | 0.15 | 0.09 | 0.09 | 0.30 | 0.16 | 0.16 | 0.22 | 0.27 | 0.22 | **0.21** |
| 06W06-30 | 0.19 | 0.25 | 0.22 | 0.21 | 0.17 | 0.17 | 0.29 | 0.15 | 0.21 | 0.20 | 0.23 | 0.19 | 0.00 | 0.28 | 0.38 | 0.30 | 0.26 | 0.26 | 0.20 | 0.22 | 0.35 | 0.19 | 0.19 | 0.28 | 0.17 | **0.23** |
| 06W06-25 | 0.20 | 0.31 | 0.36 | 0.30 | 0.39 | 0.33 | 0.08 | 0.08 | 0.19 | 0.15 | 0.13 | 0.07 | 0.00 | 0.34 | 0.22 | 0.13 | 0.07 | 0.14 | 0.09 | 0.37 | 0.20 | 0.25 | 0.25 | 0.29 | 0.26 | **0.24** |
| 06W06-45 | 0.29 | 0.82 | 0.51 | 0.46 | 0.97 | 0.11 | 0.14 | 0.20 | 0.13 | 0.22 | 0.21 | 0.22 | 0.00 | 0.23 | 0.30 | 0.21 | 0.09 | 0.06 | 0.29 | 0.14 | 0.25 | 0.08 | 0.11 | 0.11 | 0.09 | **0.33** |
| 05W05-45 | 0.44 | 0.44 | 0.54 | 0.58 | 0.17 | 0.23 | 0.23 | 0.12 | 0.34 | 0.53 | 0.40 | 0.22 | 0.00 | 0.17 | 0.43 | 0.26 | 0.12 | 0.22 | 0.24 | 0.26 | 0.28 | 0.35 | 0.33 | 0.21 | 0.24 | **0.33** |
| 05W05-0 | 0.14 | 0.10 | 0.19 | 0.06 | 0.13 | 0.15 | 0.12 | 0.15 | 0.15 | 0.13 | 0.12 | 0.13 | 0.00 | 0.14 | 0.13 | 0.18 | 0.14 | 0.16 | 0.07 | 0.13 | 0.11 | 0.11 | 0.13 | 0.13 | 0.12 | **0.13** |
| 05W05-45 | 0.44 | 0.44 | 0.54 | 0.58 | 0.17 | 0.23 | 0.23 | 0.12 | 0.34 | 0.53 | 0.40 | 0.22 | 0.00 | 0.17 | 0.43 | 0.26 | 0.12 | 0.22 | 0.24 | 0.26 | 0.28 | 0.35 | 0.33 | 0.21 | 0.24 | **0.33** |
| 05W05-25 | 0.40 | 0.37 | 0.51 | 0.54 | 0.45 | 0.44 | 0.26 | 0.54 | 0.49 | 0.35 | 0.57 | 0.31 | 0.00 | 0.32 | 0.30 | 0.27 | 0.40 | 0.31 | 0.24 | 0.24 | 0.30 | 0.32 | 0.35 | 0.32 | 0.35 | **0.38** |
| 05W03-45 | 0.15 | 0.12 | 0.08 | 0.20 | 0.39 | 0.17 | 0.21 | 0.08 | 0.09 | 0.14 | 0.33 | 0.15 | 0.00 | 0.13 | 0.12 | 0.39 | 0.29 | 0.13 | 0.25 | 0.74 | 0.21 | 0.45 | 0.25 | 0.23 | 0.74 | **0.30** |
| 05W03-25 | 0.19 | 0.16 | 0.09 | 0.12 | 0.04 | 0.10 | 0.10 | 0.06 | 0.04 | 0.09 | 0.09 | 0.09 | 0.00 | 0.07 | 0.09 | 0.12 | 0.05 | 0.06 | 0.19 | 0.12 | 0.09 | 0.09 | 0.11 | 0.08 | 0.04 | **0.10** |
| 05W03-0 | 0.23 | 0.12 | 0.14 | 0.07 | 0.16 | 0.08 | 0.04 | 0.03 | 0.13 | 0.13 | 0.13 | 0.11 | 0.00 | 0.08 | 0.08 | 0.13 | 0.11 | 0.10 | 0.11 | 0.11 | 0.17 | 0.11 | 0.01 | 0.11 | 0.08 | **0.11** |
| **Avg** | **0.22** | **0.21** | **0.20** | **0.20** | **0.24** | **0.18** | **0.17** | **0.16** | **0.17** | **0.19** | **0.20** | **0.16** | **0.00** | **0.18** | **0.20** | **0.20** | **0.15** | **0.15** | **0.17** | **0.20** | **0.19** | **0.18** | **0.16** | **0.17** | **0.20** | **0.20** |

## Gravitational Effects on Repeatability

We also have the statistics to simultaneously look at three elevations considered in the same manner. There is an issue with comparing the relative canting angles between the same heliostat at different elevation angles, which we suggest is the deflection of the mirror facets due to gravity. In [8] the authors performed modelling of NSTTF heliostats that showed a maximum displacement of 5.6 mm in the heliostat structure due to gravity. Simulation results from that paper are shown in figure 28. This translates into potential displacements of 2.0 – 2.8 mrad in the canting angles. This implies that the canting angles change slightly with the elevation angle, and that the relatively tight results for RMS error in scans at the same heliostat elevation angle can be expected to change, which is consistent with the result that we found when considering the average facet RMS data for multiple elevations, which for the 13 heliostats across all elevation angles was 0.49 mrad in facet azimuth and 1.22 mrad in facet elevation.

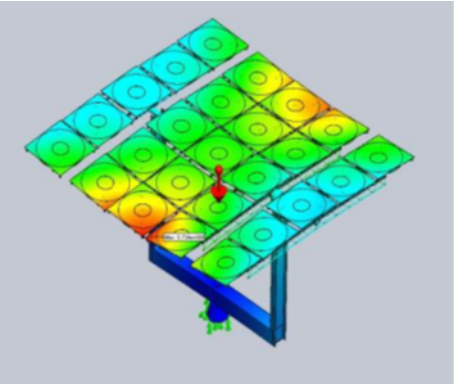

**Figure 28. Gravity deformed heliostat in horizonal orientation**

## Limits to Canting Angle Estimations

One of the primary goals of this work has been to develop a system to measure heliostat canting errors to < 0.25 mrad accuracy. The canting angle calculations are only as good as the accuracy of the plane fit. We know that, in fact, the facets do have a very slight parabolic shape. We made the planar assumption for ease in computing, as well as assuming the center of the parabola is in the center of the mirror, limiting the bias in the normal of the plane fit. We looked at several factors in our angle estimations. The first is the effect of the point density, or number of points on the facet. We simulated LiDAR scans of facets at known position and angles relative to the simulated sensor and varied the point density and range noise. Comparisons are between the input angles and calculated angles. We found that, as expected, the more points on the plane, the lower the standard deviation. Assuming the range noise to be ± 0.002 mm (the declared noise level of the scanner used), we averaged a thousand simulations at 2 mm noise and found the standard deviation for point counts between 100 and 100,000. Figure 29 plots this data. The X axis is the number of points on the facet, and the Y axis is the standard deviation of the normal expressed as the azimuth angle. The blue plot are the values calculated. The red plot is the normalized $\frac{1}{sqrt(N)}$ showing the error value does indeed follow the rule of error reduction with

increased points to analyze. Past a thousand points (0.048 mrad RMS), these numbers are significantly below the 0.25 mrad target.

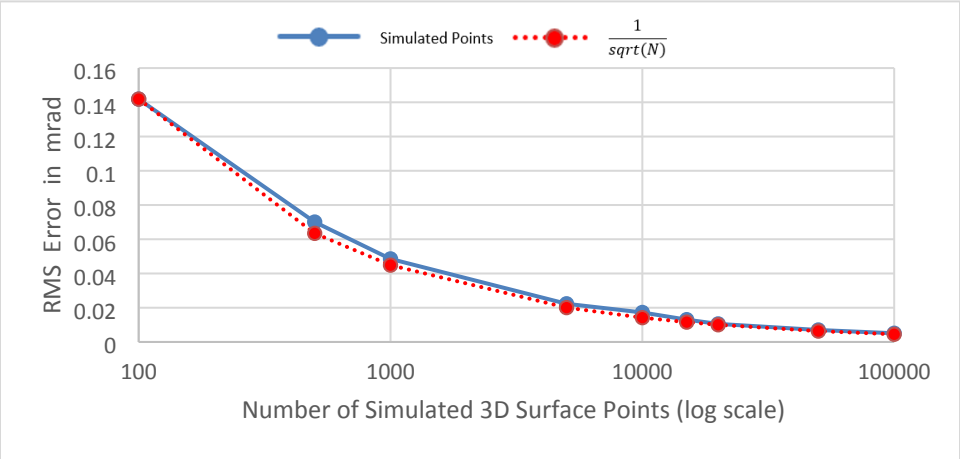


**Figure 29. Plot of RMS error versus number of scan points on the facet**

A second factor we considered here was the effect of the angle of the facet to the scanner. It was thought the larger the angle, the greater the error. The simulation testing, at straight-on to 60 degrees off-axis to the sensor showed no noticeable difference in error, showing similar standard deviation errors as the previous test; well below the target goal. While this is optimistic in terms of how the heliostat can be scanned in the field, we still assume large off-angle scanning will have a detrimental effect on accuracy. Most surfaces will have a reduction in laser intensity relative to the incident angle with the scan beam, The lower the intensity, the greater the range error. The position of the scanner relative to the heliostat will have a direct relation to this incident angle. When the scanner is close to the heliostat, this angle to the lower facets versus upper facets can vary significantly. We have not yet verified this effect in the field.

## PRODUCE A WRITTEN REPORT WITH APPROPRIATE PEER-REVIEW OF PROGRESS AND RESULTS

A paper based on the work of this project was submitted, accepted, and presented to the SolarPACES 2020 conference [9].

## CONCLUSIONS

This project considered the use of processed 3D point-cloud LiDAR scans of heliostats to calculate in-situ measurements of canting angles in the field. We have shown that LiDAR scanning is possible for valid data collection to measure heliostat facet canting angles, demonstrating this process in over two hundred field scans. We have noted the effect of facet soiling in the scanning process and have workable solutions for mirrors that are too clean. We have addressed the possibility to use either the front or back side of the heliostat for this process; however, where possible, the front side is recommended, primarily because it is unencumbered by support structures, and some heliostat designs do not expose the back-side mirror surface. We have addressed the effect of measurement noise in the calculations of plane fitting accuracy. We

were able to automate the entire remote scanning and processing from a laptop computer which can complete the entire process in less than 5 minutes per heliostat. Based on the heliostats we have tested, and the repeatability studies conducted, we believe we have achieved the 0.25 mrad error accuracy requirements given at the start of this project.

## FUTURE WORK

We initially hoped to tackle the tracking error problem by using the position data available in the scan, such as the base of the heliostat, and match it with real GPS locations. We were not at all accurate enough in our initial attempts. We assume this is because the available GPS data of heliostat positioning was itself not accurate enough to reach the desired levels of 0.5 mrad error. This needs further study to see if this, or some other method, can use readily available localization information to accomplish this task.

We do know this method is very amenable to data collection at night, or when the sun is not shining, or the heliostats are otherwise inoperable. LiDAR scanners work even better without ambient light.

### Potential for Autonomous Data Collection

It is wholly possible to mount the scanner and computer on a mobile platform and automate the entire heliostat scan process. The mobile platform would drive to a designated spot in front of each heliostat. This is very doable with path planning and collision avoidance onboard the robot to avoid driving issues. Once stationary, the platform would then initiate the scan, process the data, and then move to the next heliostat. Some coordination with the field operation to place the heliostats in an acceptable position would also be needed. LiDAR scanners have already been deployed on commercial ground and air vehicles. Figure 30 shows a recently available commercial product from FARO Technologies called Trek [10]. This places a FARO scanner, like the one we used for this project, mounted on the back of SPOT, a robotic platform from Boston Dynamics.


**Figure 30. FARO Trek; a LiDAR scanner on a mobile platform**

## ACKOWLEDGEMENTS

*The authors would like to thank the DOE Solar Energy Technology Office for supporting this research.*

## REFERENCES

1. E. Sproul, K. Chavez, J. Yellowhair, Heliostat Focusing and Canting Enhancement Technique: An Optical Heliostat Alignment Tool for the National Solar Thermal Test Facility," ES2011-54268, *Proceedings of the ASME 2011 5th International Conference on Energy Sustainability*, Washington, D.C, Aug. 7-10.
2. K. Chavez, E. Sproul, J. Yellowhair, Heliostat Facet Focusing and Characterization using the Heliostat Focusing and Canting Enhancement Technique, *Proceedings of the ASME 2012 6th International Conference on Energy Sustainability*, San Diego, CA, July 23-26.
3. J. Yellowhair, P. A. Apostolopoulos, D. E. Small, D. Novick, M. Mann, Development of an Aerial System for Heliostat Canting Assessments, *Proceedings of SolarPACES 2020 Online Conference*, Sept. 28 – Oct. 2.
4. Faro Focus 3D Scanner Website, https://www.faro.com/products/construction-bim/faro-focus/
5. CloudCompare Website, https://www.danielgm.net/cc/
6. Bounding Box Algorithm, https://github.com/GeoDaCenter/geoda/blob/master/libgdiam/README
7. SVD for plane fitting, http://math.stackexchange.com/questions/99299/best-fitting-plane-given-a-set-of-points
8. A. C. Moya, C. K. Ho, Modeling and Validation of Heliostat Deformation Due to Static Loading, Proceedings of the ASME 2011 5th International Conference on Energy Sustainability & 9th Fuel Cell Science, Engineering and Technology, August 7-10, 2011, Washington DC, USA
9. C. Q. Little, D. E. Small, Yellowhair, LiDAR For Heliostat Optical Error Assessment, *Proceedings of SolarPACES 2020 Online Conference*, Sept. 28 – Oct. 2.
10. Faro Website, https:// www.faro.com/news/faro-launches-trek-the-automated-3d-laser-scanning-integration

Sandia National Laboratories is a multimission laboratory managed and operated by National Technology & Engineering Solutions of Sandia, LLC, a wholly owned subsidiary of Honeywell International Inc., for the U.S. Department of Energy's National Nuclear Security Administration under contract DE-NA0003525.